Title

Enabling Oxidation Protection and Carrier-Type Switching for Bismuth Telluride Nanoribbons via in Situ Organic Molecule Coating.

Authors

Park, Jun

Wu, Wei

Wu, Jason

et al.

Publication Date

2023-12-11

DOI

10.1021/acs.nanolett.3c02000

Peer reviewed

NANO LETTERS

pubs.acs.org/NanoLett
Letter

Enabling Oxidation Protection and Carrier-Type Switching for Bismuth Telluride Nanoribbons via *in Situ* Organic Molecule Coating

Jun Beom Park,[#] Wei Wu,[#] Jason Yingzhi Wu, Rijan Karkee, Theresa Marie Kucinski, Karen C. Bustillo, Matthew M. Schneider, David A. Strubbe, Colin Ophus, and Michael Thompson Pettes*

Cite This: *Nano Lett.* 2023, 23, 11395−11401

ABSTRACT: Thermoelectric materials with high electrical conductivity and low thermal conductivity (e.g., Bi_2Te_3) can efficiently convert waste heat into electricity; however, in spite of favorable theoretical predictions, individual Bi_2Te_3 nanostructures tend to perform less efficiently than bulk Bi_2Te_3. We report a greater-than-order-of-magnitude enhancement in the thermoelectric properties of suspended Bi_2Te_3 nanoribbons, coated *in situ* to form a Bi_2Te_3/F_4-TCNQ core−shell nanoribbon without oxidizing the core−shell interface. The shell serves as an oxidation barrier but also directly functions as a strong electron acceptor and p-type carrier donor, switching the majority carriers from a dominant n-type carrier concentration ($\sim 10^{21}$ cm^{-3}) to a dominant p-type carrier concentration ($\sim 10^{20}$ cm^{-3}). Compared to uncoated Bi_2Te_3 nanoribbons, our Bi_2Te_3/F_4-TCNQ core−shell nanoribbon demonstrates an effective chemical potential dramatically shifted toward the valence band (by 300−640 meV), robustly increased Seebeck coefficient (~6× at 250 K), and improved thermoelectric performance (10−20× at 250 K).

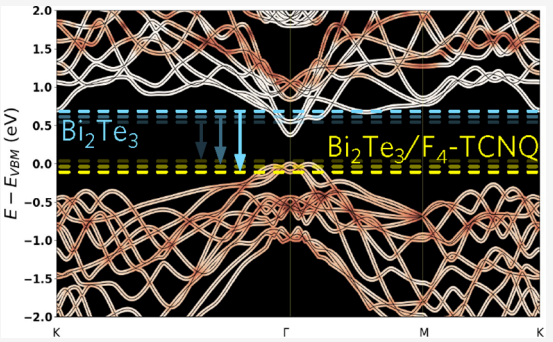

KEYWORDS: *surface doping, air-sensitive nanomaterials, thermoelectric, thermal conductivity, F4TCNQ, Bi_2Te_3*

In recent years, thermoelectric materials with high electrical conductivity and low thermal conductivity have been developed to efficiently convert waste heat into electricity,[1−3] ideally at near or above room temperature.[4−6] In particular, Bi_2Te_3 efficiently generates electrical energy from heat[6] and converts thermal energy to electricity.[7,8] Nanostructured Bi_2Te_3 has even been shown to exhibit topologically protected electronic surface states and enhanced thermoelectric characteristics.[9] Intriguingly, theoretical models have predicted that reducing the thickness of the nanostructures could lead to a significant increase in the thermoelectric figure of merit (zT).[10] However, in practice, the performance of nanostructured Bi_2Te_3 is often lower than the performance of bulk Bi_2Te_3,[2,3] most likely due to a combination of defects and impurities in the crystal structure (introduced during material growth) and surface oxidation (incurred postgrowth), which inhibit control over the chemical potential and thus the nanostructured material's thermoelectric characteristics.

Long-lasting, high-performance thermoelectric materials and devices require a manufacturing process that precisely controls the chemical potential of the nanostructured surface.[11] Consequently, researchers have explored many techniques for engineering the surface of Bi_2Te_3[12] by either generating a preoxidized surface less vulnerable to air exposure (oxygen plasma treatment),[13] improving material homogeneity and limiting surface oxidation (nonoxidizing superacid treatment,[14] applying an Al_2O_3 coating via atomic layer deposition, ALD),[12,15] or modulating the carrier concentration and chemical potential of the surface states (extrinsic doping by hole-injecting organic molecules).[16−18] While the ALD method seems to be most effective for mitigating oxidation, hole-injection of a strong p-type doping material with a high electron affinity (e.g., tetrafluorotetracyanoquinodimethane, F_4-TCNQ) has been most effective at controlling the surface potential of low-dimensional materials (e.g., ultrathin $FASnI_3$,[19] Bi_2Se_3,[20] WSe_2,[21] and Bi_2Te_3[22]). At present, the challenge is to combine these benefits and improve the performance of individual Bi_2Te_3 nanostructures to match or exceed the performance of the bulk material.

Here, we report a novel synthesis technique for preparing Bi_2Te_3/F_4-TCNQ core−shell nanoribbons that can recover the thermoelectric performance of the bulk material; our *in situ* application of a F_4-TCNQ organic barrier to a Bi_2Te_3 nanoribbon flips the major carrier from n-type to p-type (dramatically enhancing the Seebeck coefficient and zT) and

Received: May 30, 2023
Revised: November 24, 2023
Accepted: November 27, 2023
Published: December 11, 2023

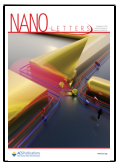

https://doi.org/10.1021/acs.nanolett.3c02000
Nano Lett. 2023, 23, 11395−11401

effectively protects the core from oxidation (no surface oxidation or loss of thermoelectric properties observed after one month in air).

Our Bi_2Te_3/F_4-TCNQ core−shell nanoribbons are synthesized using a four-step modification of an established catalyst-free chemical vapor deposition (CVD) method,[9,22] but without carrier gas and in near ultrahigh vacuum, and using a modified furnace system for the *in situ* coating (Figure 1a). (1) In a quartz tube, the growth substrate is placed roughly halfway between a bulk Bi_2Te_3 source crystal and F_4-TCNQ powder. (2) The tube is sealed and pumped to slightly better than 10^{-8} mbar. (3) To form the nanoribbon core, portable heating coils are used to heat the tube around the Bi_2Te_3 source crystal, which grows vertical nanoribbons from the growth substrate. (4) To form the shell without oxidizing the core−shell interface, near ultrahigh vacuum is maintained while the portable heating coils are moved to the F_4-TCNQ powder, which evenly coats the surface of the nanoribbons. (For additional synthesis details, see Supporting Information.)

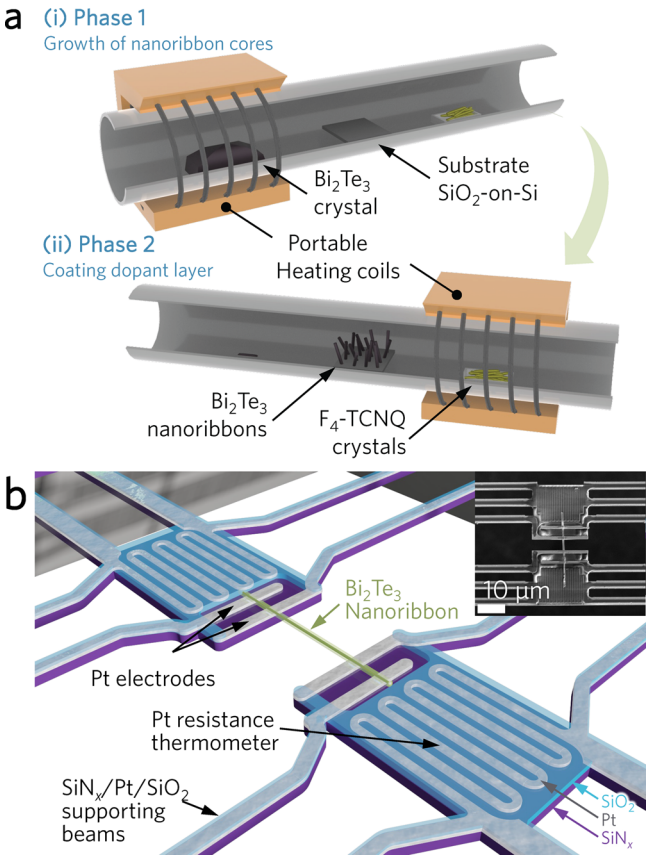

Figure 1. (a) Schematic illustration of the catalyst-free growth of Bi_2Te_3/F_4-TCNQ core−shell nanoribbons. (i) Growth of Bi_2Te_3 cores on a SiO_2-coated silicon substrate in high vacuum and (ii) *in situ* surface coating with highly electronegative molecules, achieved by reorienting the quartz tube inside the furnace without environmental exposure. (b) Schematic illustration of a nanoribbon integrated with a thermoelectric characterization device. (Inset) Top-view scanning electron microscope image of the integrated device.

To assess their respective performance, Bi_2Te_3 and Bi_2Te_3/F_4-TCNQ nanoribbons are transferred by hand (via an electrochemically sharpened tungsten probe under an optical microscope in air) to thermoelectric characterization devices (Figure 1b, inset). In each device, individual nanoribbons bridge two SiN_x membranes; both membranes are comprised of exposed Pt electrodes which connect to the nanoribbon and an insulated Pt heater/resistance thermometer (with an SiO_2 film to prevent electrical flow to the nanoribbon), and each membrane is supported by six SiN_x beams. To maximize sample contact and minimize contact resistance, top Pt−C electrodes are deposited using electron-beam-induced metal deposition inside of a scanning electron microscope (SEM). Because the transport characteristics of Bi_2Te_3 are driven by a combination of bulk conduction and surface transport, we selected nanoribbons with similar thicknesses and widths to minimize the surface transport variability and better reveal the effective chemical potential change enabled by the shell.

We begin characterization by assessing the general morphology of the nanoribbons via transmission electron microscopy (TEM, image-corrected FEI Titan 80-300, operating at 300 kV), using established experimental and computational postprocessing routines[23−25] to show that the Bi_2Te_3/F_4-TCNQ nanoribbons are completely coated and that both the Bi_2Te_3 and Bi_2Te_3/F_4-TCNQ nanoribbons are straight single crystals (Figure 2a). Atomic force microscopy (AFM, Bruker Dimension Icon) is used to measure rectangular cross sections and suspended lengths of the Bi_2Te_3 (632 nm × 53 ± 2 nm × 3.89 μm) and the Bi_2Te_3/F_4-TCNQ (794 nm × 269 ± 42 nm × 4.44 μm) core−shell nanoribbons (Figure S1,

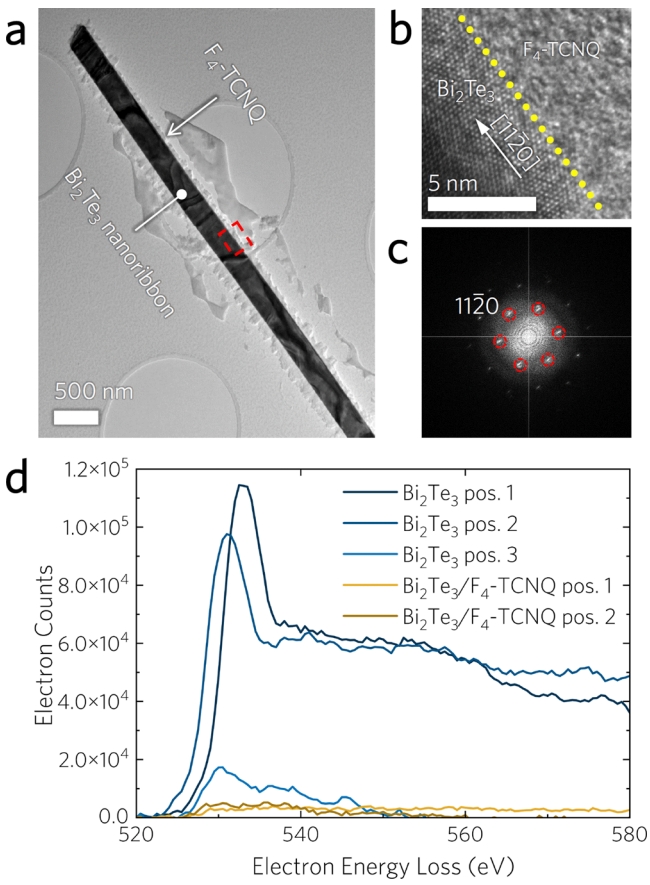

Figure 2. TEM analysis of a Bi_2Te_3/F_4-TCNQ core−shell interface shows (a) a thin F_4-TCNQ shell layer fully covering the Bi_2Te_3 nanoribbons and (b) indication of an oxide-free Bi_2Te_3/F_4-TCNQ interface in the region indicated by the red box in panel a. (c) FFT of panel b. (d) Electron energy loss spectroscopy at the O K-edge for the uncoated (blue lines) and coated (tan lines) nanoribbons.

https://doi.org/10.1021/acs.nanolett.3c02000
Nano Lett. 2023, 23, 11395−11401

Supporting Information). The TEM image of the interfacial region shows a clean structural contrast between the atomically ordered Bi_2Te_3 core and amorphous F_4-TCNQ shell (Figure 2b), with no evidence of unintentional interface oxidation (as reported for previous synthesis methods).[26] The corresponding fast Fourier transform (FFT) pattern confirms that the Bi_2Te_3 nanoribbon has a clear $[11\bar{2}0]$ crystal growth orientation (Figure 2c).

A precise thickness measurement is required for modeling transport characteristics (e.g., electrical and thermal conductivity), but the thick F_4-TCNQ coating prevents us from directly obtaining the thickness of the Bi_2Te_3/F_4-TCNQ via AFM. Therefore, we estimate sample thickness using the log-ratio technique, where λ is the inelastic mean free path (in this case, of Bi and Te),[27] and t/λ represents the mean number of scattering events. To calculate the thickness of the coating, we substituted organic compounds (Kapton and adenine) with mass densities similar to F_4-TCNQ and estimated the thickness of the Bi_2Te_3 nanoribbon (40 ± 6 nm) and Bi_2Te_3/F_4-TCNQ nanoribbon (116 ± 13 nm Bi_2Te_3 core, 203 ± 30 nm Bi_2Te_3/F_4-TCNQ core–shell), achieving relatively good agreement with the AFM measurements. (We use this total thickness for conductivity calculations, except where noted.)

After the samples have been exposed to air for more than a month, we use electron energy loss spectroscopy (EELS) and energy dispersive X-ray spectroscopy (EDS) to look for oxygen and fluorine, respectively. EELS spectra obtained from several locations on the Bi_2Te_3 and Bi_2Te_3/F_4-TCNQ nanoribbons reveals that the Bi_2Te_3 nanoribbons have a greater oxygen presence (Figure 2d), which we attribute to surface oxidation in the uncoated sample. Additional EELS spectra (Figure S2, Supporting Information) show a greater oxygen K-edge peak present for the Bi_2Te_3 nanoribbon than the Bi_2Te_3/F_4-TCNQ core–shell nanoribbon, which is indicative of the effectiveness of the latter's oxidation barrier shell. EDS spectra confirm the presence of fluorine from the shell (Figure S3, Supporting Information).

To quantitatively evaluate the crystal quality of the core–shell nanostructure over a larger length scale and discover whether it is free from precipitate phases, we also performed quantitative electron diffraction. Our TEM analysis of the Bi_2Te_3/F_4-TCNQ nanoribbons' microstructural characteristics shows a bright field (BF) image captured near the middle of the core–shell nanoribbon, clearly showing the conformal F_4-TCNQ shell (~55 nm-thick) coating the Bi_2Te_3 core (Figure 3a). The ordered selected area electron diffraction pattern (Figure 3b) confirms that the nanoribbon crystal orientation is clearly aligned to the $[11\bar{2}0]$ direction, the zone axis is along [0001], and there are no unwanted crystal structures within the nanoribbon. (Note: we compensate for imperfect alignment of the condenser, objective, and projector lens systems by performing elliptical correction). Figure 3c presents the weighted radial histogram of the found Bragg peaks, the reciprocal space scattering vector q, and (for reference) the expected positions of the peaks for Bi_2Te_3.[28] The sharp $(11\bar{2}0)$ peak clearly matches the database value, providing strong evidence that our Bi_2Te_3/F_4-TCNQ nanoribbons are highly oriented. The only unexpected peaks are the forbidden reflections caused by point defects in the nanoribbon core (as calculated from the Bi_2Te_3 $(30\bar{3}0)$ reflection and marked with a † in Figure 3c), indicating that our coating process generates no unintended crystalline phases, minimizing the risk

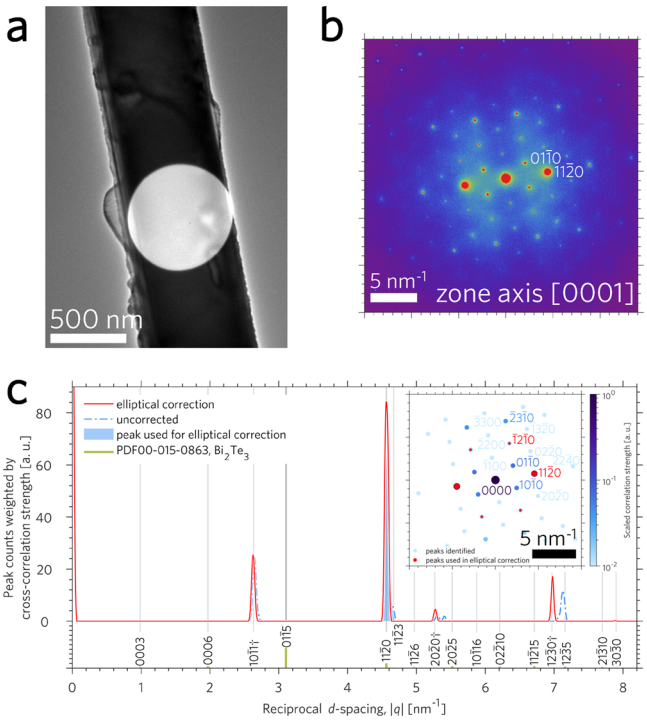

Figure 3. Quantitative electron diffraction analysis of the Bi_2Te_3/F_4-TCNQ core–shell nanoribbon on a thermoelectric characterization device. (a) Double-exposure TEM image, indicating the diffraction collection region. (b) Selected area electron diffraction pattern. (c) Weighted radial histogram of the peak positions before (blue dash-dot line) and after (red solid line) elliptical correction; for comparison, the expected histogram for bulk Bi_2Te_3 is included (vertical solid lines;[28] † indicates X-ray-forbidden reflections derived from the $(3\bar{0}0)$ reflection). (c, inset) Peak location map aligned to the $[10\bar{1}0]$ reflection, indicating the peaks used in the elliptical correction algorithm (red circles) to correct for inherent slight misalignments in the condenser, objective, and projector lens systems.

of unpredictable transport behavior or thermoelectric properties.[15] (For the angular histogram, see Figure S4, Supporting Information.)

We then experimentally assess the Seebeck coefficient and electrical conductivity of each nanoribbon as a function of the temperature (Figure 4a,b). The Bi_2Te_3 nanoribbon exhibits a negative Seebeck coefficient that decreases steadily (−4 to −22 $\mu V\ K^{-1}$) as temperatures increase (30–250 K); in contrast, the Bi_2Te_3/F_4-TCNQ nanoribbon shows a dramatically positive Seebeck coefficient (12–127 $\mu V\ K^{-1}$) over the same interval, strongly suggesting a conversion of the main carrier from n-type to p-type. We are able to validate that finding computationally, showing that, whereas the Bi_2Te_3 nanoribbon has high n-type carrier concentration ($\sim 10^{21}$ cm^{-3}), the Bi_2Te_3/F_4-TCNQ nanoribbon has a high p-type carrier concentration of ($\sim 10^{20}$ cm^{-3}) and outperforms the Bi_2Te_3 nanoribbon by at least 3.0× over the entire measured temperature range (30–250 K) and 5.8–6.0× at 150–250 K [for the full range plot of $S(T)$ versus carrier concentration, see Figure S5, Supporting Information]. As the temperature rises from 7–380 K, the electrical conductivity of the Bi_2Te_3 nanoribbon decreases [$(2.3–1.5) \times 10^5$ S m^{-1}]; because the Bi_2Te_3/F_4-TCNQ nanoribbon has an order-of-magnitude lower carrier concentration, the Bi_2Te_3/F_4-TCNQ nanoribbon's highest electrical conductivity [$(0.76–0.12) \times 10^5$ S

https://doi.org/10.1021/acs.nanolett.3c02000
Nano Lett. 2023, 23, 11395−11401

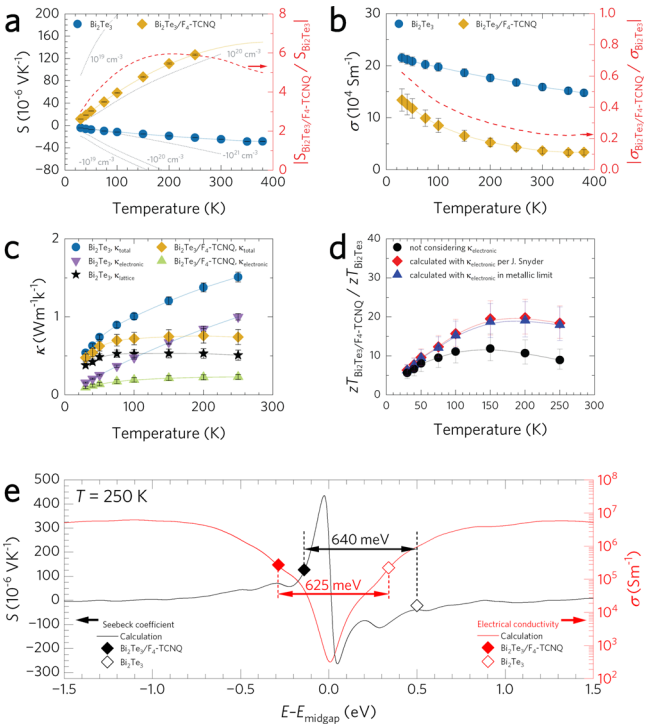

Figure 4. Temperature-dependent thermoelectric properties of Bi_2Te_3 and Bi_2Te_3/F_4-TCNQ-nanoribbons. (a) Comparison of theoretical calculation and measured Seebeck coefficient S. (b) Measured electrical conductivity σ as a function of temperature. For comparison, the Bi_2Te_3/F_4-TCNQ:Bi_2Te_3 ratios are shown as dashed red lines in both panels. (c) Plots of total (κ_{total}), lattice ($\kappa_{lattice}$), and electronic ($\kappa_{electronic}$) thermal conductivity of the Bi_2Te_3 and Bi_2Te_3/F_4-TCNQ nanoribbons. The κ_{total} of the Bi_2Te_3 nanoribbon was experimentally obtained and separated into $\kappa_{electronic}$ (the mean values obtained using Snyder's formula[30] and the metallic limit for Lorenz number) and $\kappa_{lattice}$. Then, the $\kappa_{electronic}$ of Bi_2Te_3/F_4-TCNQ nanoribbon was similarly calculated, and κ_{total} was estimated assuming $\kappa_{lattice}$ obtained for the Bi_2Te_3 nanoribbon and the total Bi_2Te_3/F_4-TCNQ cross sectional area. (d) Plots of three different estimations for the enhancement ratio of thermoelectric figure of merit, $zT = (S^2\sigma/\kappa_{total})T$, for both the Bi_2Te_3 and Bi_2Te_3/F_4-TCNQ nanoribbons: (1) the ratio of zT assumes the same κ_{total} for both the Bi_2Te_3 and Bi_2Te_3/F_4-TCNQ (black circles); (2, 3) the $\kappa_{electronic}$ is estimated with a Lorenz number calculated either by using Snyder's model[30] (red diamonds) or assuming the metallic limit (blue triangles). (e) Intersections of the measured S (black diamonds) and σ (red diamonds) at 250 K with the calculated S (black line) and σ (red line) as a function of chemical potential with respect to the middle of the electronic band gap.

m^{-1}] is comparable to the Bi_2Te_3 nanoribbon's lowest electrical conductivity.

The thermoelectric figure of merit $zT = [S^2\sigma/(\kappa_{lattice} + \kappa_{electronic})]T$ is more challenging to compare, but we begin by calculating the total thermal conductivity (κ_{total}) of the uncoated Bi_2Te_3 nanoribbon following an established bipolar direct current reversal technique[29] and then determined the electronic contribution via the Wiedemann–Franz law $\kappa_{electronic} = \sigma LT$:

$$\kappa_{total} = \kappa_{lattice} + \kappa_{electronic} \quad (1a)$$

$$= \kappa_{lattice} + \sigma LT \quad (1b)$$

$$\kappa_{lattice} = \kappa_{total} - \sigma LT \quad (1c)$$

where T is the absolute temperature, L is the Lorenz number, $\kappa_{lattice}$ is the lattice contribution to the thermal conductivity, and $\kappa_{electronic}$ is the electronic contribution to the thermal conductivity. To assess the validity of our $\kappa_{electronic}$ calculation and allow us to better quantify the uncertainty in zT, we use three different methods for calculating L (each based on somewhat different assumptions). The first two calculate approximations of L based on the state of electrons in the material: the free electron model (i.e., the metallic limit) system uses the Sommerfeld value $L_0 = \pi^2 k_B^2/(3e^2) = 2.44 \times 10^{-8}$ W Ω K^{-2}, which approximates well in the highly doped regime;[9] whereas the Snyder method[30] uses the Seebeck coefficient, $L = (1.5 + \exp[|S|/116]) \times 10^{-8}$ W Ω K^{-2}, with S given in units of μV K^{-1}, and approximates well for nondegenerate semiconductors. For this work, we also obtain a more precise zT by running a DFT simulation to calculate $\kappa_{electronic}$ using the chemical potential corresponding to the measured electrical conductivity: $\kappa_{electronic}(T = 250\ K)$. The DFT calculated $\kappa_{electronic}$ (1.13 W m^{-1} K^{-1}) is somewhat higher than the metallic limit (1.02 ± 0.04) and Snyder model (0.98 ± 0.04 W m^{-1} K^{-1}) results, which suggest that both common approximations may slightly underestimate $\kappa_{electronic}$. Unfortunately, we cannot directly calculate the κ_{total} of the Bi_2Te_3/F_4-TCNQ nanoribbon. However, X-ray photoelectron spectroscopy analysis indicates that F_4-TCNQ molecules with a thickness exceeding 2 nm do not have a significant impact on charge transfer;[31,32] thus, in the future, if the shell can be as synthesized to be ≤2 nm, we will be able to estimate the κ_{total} of the Bi_2Te_3/F_4-TCNQ nanoribbon conservatively by using the cross-sectional area of the Bi_2Te_3, plus the cross-sectional area of the F_4-TCNQ shell. We can then calculate $\kappa_{lattice}$ of the Bi_2Te_3 nanoribbon and then adding $\kappa_{lattice}$ to the calculated $\kappa_{electronic}$ of the Bi_2Te_3/F_4-TCNQ nanoribbon. Even so, the preliminary data suggest that even the relatively thick shell

Table 1. Summary of the zT Enhancement of the Bi_2Te_3 and Bi_2Te_3/F_4-TCNQ Nanoribbons[a]

	maximum zT enhancement (T = 150–200 K)			zT enhancement (T = 250 K)		
model for $\kappa_{electronic}$	zT of Bi_2Te_3	zT of Bi_2Te_3/F_4-TCNQ[b]	zT ratio at temp	zT of Bi_2Te_3	zT of Bi_2Te_3/F_4-TCNQ[b]	zT ratio
Metallic limit, $L = 2.44 \times 10^{-8}$ W Ω K^{-1}	$8.8 \times 10^{-3} \pm 9.3 \times 10^{-4}$	$1.7 \times 10^{-1} \pm 0.4 \times 10^{-2}$	19.1 ± 6.6, 200 K	$1.3 \times 10^{-2} \pm 1.4 \times 10^{-3}$	$2.3 \times 10^{-1} \pm 5.7 \times 10^{-2}$	18.0 ± 6.2
Snyder's method,[40] $L = (1.5 + \exp[\|S\|/116]) \times 10^{-8}$ W Ω K	$8.8 \times 10^{-3} \pm 9.3 \times 10^{-4}$	$1.7 \times 10^{-1} \pm 3.9 \times 10^{-2}$	19.8 ± 6.6, 200 K	$1.3 \times 10^{-2} \pm 1.4 \times 10^{-3}$	$2.4 \times 10^{-1} \pm 5.4 \times 10^{-2}$	18.4 ± 6.2
Negligible electronic contribution, $1 \gg \kappa_{electronic}/\kappa_{lattice}$	$5.2 \times 10^{-3} \pm 5.5 \times 10^{-4}$	$6.2 \times 10^{-2} \pm 1.1 \times 10^{-2}$	11.9 ± 3.4, 150 K	$1.3 \times 10^{-2} \pm 1.4 \times 10^{-3}$	$1.2 \times 10^{-1} \pm 2.1 \times 10^{-2}$	8.9 ± 2.6

[a]The lattice contribution to the thermal conductivity has been calculated as $\kappa - \sigma LT$, where L is obtained with two different models based on the measured thermoelectric properties. The maximum zT (between 150 and 200 K) is shown for each sample, alongside their respective zT at 250 K. [b]Estimated from measurement values.

https://doi.org/10.1021/acs.nanolett.3c02000
Nano Lett. 2023, 23, 11395–11401

(~55 nm) of our Bi_2Te_3/F_4-TCNQ nanoribbon can be modeled as having the same properties as the nanostructured core.[19,33]

To estimate the potential utility of this material for thermoelectric applications, we also plot the thermal conductivities (separated according to the mean value of the metallic limit and Snyder model results[9,30] in Figure 4c; full calculations in Figure S7, Supporting Information). To better assess the confidence bounds, we also plot the enhancement ratio of the zT of the Bi_2Te_3/F_4-TCNQ nanoribbon, calculated via the metallic limit, Snyder model, and our DFT method (assuming $\kappa_{electronic}/\kappa_{lattice} \ll 1$) (Figure 4d). The zT ratio enhancement is calculated as

$$\frac{zT_2}{zT_1} = \frac{\frac{S_2^2\sigma_2}{\kappa_{lattice}+\kappa_{electronic,2}}}{\frac{S_1^2\sigma_1}{\kappa_{lattice}+\kappa_{electronic,1}}} \tag{2a}$$

$$= \frac{S_2^2\sigma_2/(1+\sigma_2 L_2 T/\kappa_{lattice})}{S_1^2\sigma_1/(1+\sigma_1 L_1 T/\kappa_{lattice})} \tag{2b}$$

$$\approx \frac{S_2^2\sigma_2}{S_1^2\sigma_1}, \text{ when } \frac{\kappa_{electronic}}{\kappa_{lattice}} \ll 1 \tag{3}$$

The individual zT calculations for the Bi_2Te_3 and Bi_2Te_3/F_4-TCNQ nanoribbons are plotted in Table 1; notably, all methods show significantly (10−20×) higher zT values for Bi_2Te_3/F_4-TCNQ. Together, these data give us a reasonable estimate of the lower confidence bound.

To get the higher confidence bound, we also estimate the upper limit of zT enhancements using the EELS-estimated thickness of the nanoribbon core. Assuming a negligibly thin F_4-TCNQ shell, we predict that an optimized Bi_2Te_3/F_4-TCNQ nanoribbon will outperform the zT of the Bi_2Te_3 nanoribbon by 20−33× (Figure S8, Supporting Information). We attribute this gain to the fact that while the negligibly thin F_4-TCNQ shell will still lower the electrical conductivity of the Bi_2Te_3 nanoribbon,[34] the slimmer shell profile maintains the surface charge transport (and, thus, surface doping), while still preventing oxidation. Previous attempts to significantly enhance the zT of Bi_2Te_3 by other methods[35,22] consistently yielded low (<0.2) zT values below room temperature, with similarly low zT outcomes reported for the optimized Bi_2Te_3 samples at (or below) room temperature.[2,36] However, preliminary calculations suggest that an optimized Bi_2Te_3/F_4-TCNQ nanoribbon will achieve $zT \sim 0.25$ at 250 K.

We then push further into the fundamental physics that govern the performance of the nanoribbons. Since the position of the chemical potential governs thermoelectric performance, we compare the quantitative effective chemical potential calculations and the measured thermoelectric properties of the Bi_2Te_3 and Bi_2Te_3/F_4-TCNQ nanoribbons (Figure 4e; orbital projected electronic band structure and density of states, Figure S5, Supporting Information). We also used our calculation results to approximate the Bi_2Te_3/F_4-TCNQ nanoribbons assuming the rigid band approximation. We can now leverage the calculation of the electronic bandstructure to calculate the shift from n-type to p-type carrier donors between the Bi_2Te_3 and the Bi_2Te_3/F_4-TCNQ nanoribbons. Figure 4e plots the intersections of the experimental Seebeck coefficient and electrical conductivity measured at 250 K from Bi_2Te_3 and Bi_2Te_3/F_4-TCNQ nanoribbons with the theoretically obtained curves. Using these measured values, we can estimate the range of effective surface potential shift by extrinsic p-type dopant coating to be between 625−640 meV.

To further understand variation of *ab initio* models on the chemical potential shift due to F4-TCNQ, we compare our experimental results with a previously reported calculation based on the Landauer formalism,[9] which indicates a very different effective chemical potential shift of 300−355 meV (Figure S8, Supporting Information). We note that multiple challenges also remain: the damage caused by surface oxidation is subtle and may only be detectible with precision techniques, such as angle-resolved photoemission spectroscopy (ARPES),[12] and research on the effects of thermoelectric transport in one-dimensional materials is still in its early stage.[21,35,37] Additionally, the fact that two different first-principles models produce two very different values of effective chemical potential shift means that these models are not fully capturing the exact interfacial mechanisms that lead to experimental observables, and thus, the models need further improvements by the theory community.

In conclusion, we report a novel method for synthesizing Bi_2Te_3/F_4-TCNQ core−shell nanoribbons *in situ* using catalyst-free high vacuum synthesis to enhance oxidation resistance and improve thermoelectric properties. Extensive characterization of the Bi_2Te_3 core showed highly oriented crystal structures with growth along the $[11\bar{2}0]$ direction, without the diffraction peak position change or broadening that would indicate reaction with the amorphous F_4-TCNQ shell. Even after a month-long exposure to air, the Bi_2Te_3/F_4-TCNQ interface showed no observable oxide shell formation. Experimental thermoelectric assessment of Bi_2Te_3 and Bi_2Te_3/F_4-TCNQ nanoribbons demonstrate an improvement in Seebeck coefficient from ~20 to ~125 $\mu V\ K^{-1}$ at 250 K and more than an order of magnitude higher zT. A combination of simulation and experimental measurement suggests that the F_4-TCNQ shell shifts the nanoribbon to a dominantly p-type majority carrier, enhancing the surface potential of the nanoribbon by 625−640 and 300−355 meV when calculated by two different *ab initio* models. Our *in situ* growth technique enables the synthesis of enhanced, long-lasting thermoelectric nanoribbons, with numerous potential applications in microelectronic and thermoelectric devices. Critically, this technique is also generalizable for surface doping other air-sensitive nanomaterials. We note that additional characterization techniques (e.g., infrared spectroscopy near the C≡N peak of F_4-TCNQ) have the potential to yield additional information about the oxidation state of the coating[38] in future work in this field. Together these characterizations and calculations provide strong evidence for a path to high performance thermoelectric nanostructures through the use of *in situ* organic molecule coatings, which is valuable for future 1D-based thermoelectric and microelectronics applications.[23,39−41]

■ ASSOCIATED CONTENT

Data Availability Statement

The data that support the plots in the manuscript are available from the corresponding author upon reasonable request.

Supporting Information

The Supporting Information is available free of charge at https://pubs.acs.org/doi/10.1021/acs.nanolett.3c02000.

https://doi.org/10.1021/acs.nanolett.3c02000
Nano Lett. 2023, 23, 11395−11401

Additional characterization and analysis results for atomic force microscopy, transmission electron microscopy, additional theoretical calculations, additional thermoelectric and transport data, and comparison of data with an additional theoretical model based on the Landauer approach (PDF)

AUTHOR INFORMATION

Corresponding Author

Michael Thompson Pettes − *Center for Integrated Nanotechnologies (CINT), Materials Physics and Applications Division, Los Alamos National Laboratory, Los Alamos, New Mexico 87545, United States;* orcid.org/0000-0001-6862-6841; Email: pettesmt@lanl.gov

Authors

Jun Beom Park − *Center for Integrated Nanotechnologies (CINT), Materials Physics and Applications Division, Los Alamos National Laboratory, Los Alamos, New Mexico 87545, United States*

Wei Wu − *Department of Mechanical Engineering and Institute of Materials Science, University of Connecticut, Storrs, Connecticut 06269, United States*

Jason Yingzhi Wu − *Department of Mechanical Engineering and Institute of Materials Science, University of Connecticut, Storrs, Connecticut 06269, United States*

Rijan Karkee − *Center for Integrated Nanotechnologies (CINT), Materials Physics and Applications Division, Los Alamos National Laboratory, Los Alamos, New Mexico 87545, United States; Department of Physics, University of California, Merced, California 95343, United States;* orcid.org/0000-0003-0124-5213

Theresa Marie Kucinski − *Center for Integrated Nanotechnologies (CINT), Materials Physics and Applications Division, Los Alamos National Laboratory, Los Alamos, New Mexico 87545, United States*

Karen C. Bustillo − *National Center for Electron Microscopy (NCEM), Molecular Foundry, Lawrence Berkeley National Laboratory, Berkeley, California 94720, United States;* orcid.org/0000-0002-2096-6078

Matthew M. Schneider − *Center for Integrated Nanotechnologies (CINT), Materials Physics and Applications Division and Materials Science in Radiation and Dynamics Extremes (MST-8), Materials Science and Technology Division, Los Alamos National Laboratory, Los Alamos, New Mexico 87545, United States*

David A. Strubbe − *Department of Physics, University of California, Merced, California 95343, United States;* orcid.org/0000-0003-2426-5532

Colin Ophus − *National Center for Electron Microscopy (NCEM), Molecular Foundry, Lawrence Berkeley National Laboratory, Berkeley, California 94720, United States*

Complete contact information is available at: https://pubs.acs.org/10.1021/acs.nanolett.3c02000

Author Contributions

#J.B.P. and W.W. contributed equally. M.T.P. conceived and led the project. M.T.P., W.W., K.C.B., M.S., and C.O. performed TEM and computational microscopy analysis. W.W., J.Y.W., and M.T.P. performed sample synthesis and sample measurement. J.B.P. and T.M.K. performed AFM measurements. J.B.P., R.K., and M.T.P. performed data analysis. R.K. and D.A.S. designed and performed all theoretical calculations and modeling. The manuscript was written by J.B.P. and M.T.P. with input and intellectual contributions from all coauthors.

Notes

The authors declare no competing financial interest.

ACKNOWLEDGMENTS

This work was supported by the Laboratory Directed Research and Development program of Los Alamos National Laboratory under Projects 20230014DR (M.T.P., J.B.P., R.K.), 20220485MFR (M.T.P., T.M.K., M.S.), and 20190516ECR (M.T.P.). D.A.S. was supported by the U.S. Department of Energy, National Nuclear Security Administration, Minority Serving Institution Partnership Program, under Award DE-NA0003984. Work at the Molecular Foundry was supported by the Office of Science, Office of Basic Energy Sciences, of the U.S. Department of Energy under Contract DE-AC02-05CH11231. C.O. acknowledges additional support from the U.S. Department of Energy Early Career Research Award program. This work was performed in part at the Center for Integrated Nanotechnologies, an Office of Science User Facility operated for the U.S. Department of Energy (DOE) Office of Science. Los Alamos National Laboratory, an affirmative action equal opportunity employer, is managed by Triad National Security, LLC for the U.S. Department of Energy's NNSA, under Contract 89233218CNA000001.

REFERENCES

(1) Zhang, Q. H.; Huang, X. Y.; Bai, S. Q.; Shi, X.; Uher, C.; Chen, L. D. Thermoelectric devices for power generation: Recent progress and future challenges. *Adv. Eng. Mater.* **2016**, *18*, 194−213.

(2) Yazdani, S.; Pettes, M. T. Nanoscale self-assembly of thermoelectric materials: A review of chemistry-based approaches. *Nanotechnology* **2018**, *29*, 432001.

(3) Chen, R.; Lee, J.; Lee, W.; Li, D. Thermoelectrics of nanowires. *Chem. Rev.* **2019**, *119*, 9260−9302.

(4) Nolas, G. S.; Sharp, J.; Goldsmid, H. J. *Thermoelectrics: Basic Principles and New Materials Developments*; Springer-Verlag: Heidelberg, Germany, 2001.

(5) Rowe, D. M. *CRC Handbook of Thermoelectrics: Macro to Nano*; CRC Press/Taylor & Francis: New York, 2006.

(6) Mao, J.; Liu, Z.; Zhou, J.; Zhu, H.; Zhang, Q.; Chen, G.; Ren, Z. Advances in thermoelectrics. *Adv. Phys.* **2018**, *67*, 69−147.

(7) Hegde, G. S.; Prabhu, A. N. A review on doped/composite bismuth chalcogenide compounds for thermoelectric device applications: Various synthesis techniques and challenges. *J. Electron. Mater.* **2022**, *51*, 2014−2042.

(8) Tang, J.; Chen, Y.; McCuskey, S. R.; Chen, L.; Bazan, G. C.; Liang, Z. Recent advances in n-type thermoelectric nanocomposites. *Adv. Electron. Mater.* **2019**, *5*, No. 1800943.

(9) Pettes, M. T.; Maassen, J.; Jo, I.; Lundstrom, M. S.; Shi, L. Effects of surface band bending and scattering on thermoelectric transport in suspended bismuth telluride nanoplates. *Nano Lett.* **2013**, *13*, 5316−5322.

(10) Ghaemi, P.; Mong, R. S. K.; Moore, J. E. In-plane transport and enhanced thermoelectric performance in thin films of the topological insulators Bi_2Te_3 and Bi_2Se_3. *Phys. Rev. Lett.* **2010**, *105*, No. 166603.

(11) Lang, M.; He, L.; Xiu, F.; Yu, X.; Tang, J.; Wang, Y.; Kou, X.; Jiang, W.; Fedorov, A. V.; Wang, K. L. Revelation of Topological Surface States in Bi_2Se_3 Thin Films by In Situ Al Passivation. *ACS Nano* **2012**, *6*, 295−302.

(12) Chen, C.; He, S.; Weng, H.; Zhang, W.; Zhao, L.; Liu, H.; Jia, X.; Mou, D.; Liu, S.; He, J.; Peng, Y.; Feng, Y.; Xie, Z.; Liu, G.; Dong, X.; Zhang, J.; Wang, X.; Peng, Q.; Wang, Z.; Zhang, S.; Yang, F.; Chen, C.; Xu, Z.; Dai, X.; Fang, Z.; Zhou, X. J. Robustness of

topological order and formation of quantum well states in topological insulators exposed to ambient environment. *Proc. Natl. Acad. Sci. U. S. A.* **2012**, *109*, 3694−3698.
(13) Dhall, R.; Li, Z.; Kosmowska, E.; Cronin, S. B. Charge neutral MoS_2 field effect transistors through oxygen plasma treatment. *J. Appl. Phys.* **2016**, *120*, No. 195702.
(14) Amani, M.; Lien, D.-H.; Kiriya, D.; Xiao, J.; Azcatl, A.; Noh, J.; Madhvapathy, S. R.; Addou, R.; KC, S.; Dubey, M.; Cho, K.; Wallace, R. M.; Lee, S.-C.; He, J.-H.; Ager, J. W.; Zhang, X.; Yablonovitch, E.; Javey, A. Near-unity photoluminescence quantum yield in MoS_2. *Science* **2015**, *350*, 1065−1068.
(15) Chen, J.; Kim, J.; Poudel, N.; Hou, B.; Shen, L.; Shi, H.; Shi, L.; Cronin, S. B. Enhanced thermoelectric efficiency in topological insulator Bi_2Te_3 nanoplates via atomic layer deposition-based surface passivation. *Appl. Phys. Lett.* **2018**, *113*, No. 083904.
(16) Hwang, J.; Wan, A.; Kahn, A. Energetics of metal−organic interfaces: New experiments and assessment of the field. *Mater. Sci. Eng. R* **2009**, *64*, 1−31.
(17) Coletti, C.; Riedl, C.; Lee, D. S.; Krauss, B.; Patthey, L.; von Klitzing, K.; Smet, J. H.; Starke, U. Charge neutrality and band-gap tuning of epitaxial graphene on SiC by molecular doping. *Phys. Rev. B* **2010**, *81*, No. 235401.
(18) Robertson, J. Band offsets, Schottky barrier heights, and their effects on electronic devices. *J. Vac. Sci. Technol. A* **2013**, *31*, No. 050821.
(19) Zheng, L.; Zhu, T.; Li, Y.; Wu, H.; Yi, C.; Zhu, J.; Gong, X. Enhanced thermoelectric performance of F4-TCNQ doped $FASnI_3$ thin films. *J. Mater. Chem. A* **2020**, *8*, 25431−25442.
(20) Kim, D.; Cho, S.; Butch, N. P.; Syers, P.; Kirshenbaum, K.; Adam, S.; Paglione, J.; Fuhrer, M. S. Surface conduction of topological Dirac electrons in bulk insulating Bi_2Se_3. *Nat. Phys.* **2012**, *8*, 459−463.
(21) Pan, Y.; Hong, G.; Raja, S. N.; Zimmermann, S.; Tiwari, M. K.; Poulikakos, D. Significant thermal conductivity reduction of silicon nanowire forests through discrete surface doping of germanium. *Appl. Phys. Lett.* **2015**, *106*, No. 093102.
(22) Pettes, M. T.; Kim, J.; Wu, W.; Bustillo, K. C.; Shi, L. Thermoelectric transport in surface- and antimony-doped bismuth telluride nanoplates. *APL Mater.* **2016**, *4*, No. 104810.
(23) Londoño-Calderon, A.; Dhall, R.; Ophus, C.; Schneider, M. M.; Wang, Y.; Dervishi, E.; Kang, H. S.; Lee, C.-H.; Yoo, J.; Pettes, M. T. Visualizing grain statistics in MOCVD WSe_2 through four-dimensional scanning transmission electron microscopy. *Nano Lett.* **2022**, *22*, 2578−2585.
(24) Londoño-Calderon, A.; Williams, D. J.; Ophus, C.; Pettes, M. T. 1D to 2D transition in tellurium observed by 4D electron microscopy. *Small* **2020**, *16*, No. 2005447.
(25) Pekin, T. C.; Gammer, C.; Ciston, J.; Minor, A. M.; Ophus, C. Optimizing disk registration algorithms for nanobeam electron diffraction strain mapping. *Ultramicroscopy* **2017**, *176*, 170−176.
(26) Jauregui, L. A.; Pettes, M. T.; Rokhinson, L. P.; Shi, L.; Chen, Y. P. Gate tunable relativistic mass and Berry's phase in topological insulator nanoribbon field effect devices. *Sci. Rep.* **2015**, *5*, 8452.
(27) Iakoubovskii, K.; Mitsuishi, K.; Nakayama, Y.; Furuya, K. Mean free path of inelastic electron scattering in elemental solids and oxides using transmission electron microscopy: Atomic number dependent oscillatory behavior. *Phys. Rev. B* **2008**, *77*, No. 104102.
(28) Swanson, H. E.; Morris, M. C.; Evans, E. H.; Ulmer, L. Section 3—Data for 51 Substances. In *NBS Monograph 25: Standard X-ray Diffraction Powder Patterns*; U. S. Department of Commerce, National Bureau of Standards: Washington, DC, 1964; p 64.
(29) Wu, J. Y.; Wu, W.; Pettes, M. T. Ultra-high resolution steady-state micro-thermometry using a bipolar direct current reversal technique. *Rev. Sci. Instrum.* **2016**, *87*, No. 094901.
(30) Kim, H.-S.; Gibbs, Z. M.; Tang, Y.; Wang, H.; Snyder, G. J. Characterization of Lorenz number with Seebeck coefficient measurement. *APL Mater.* **2015**, *3*, No. 041506.
(31) Yuan, G. D.; Ng, T. W.; Zhou, Y. B.; Wang, F.; Zhang, W. J.; Tang, Y. B.; Wang, H. B.; Luo, L. B.; Wang, P. F.; Bello, I.; Lee, C. S.; Lee, S. T. p-type conductivity in silicon nanowires induced by heterojunction interface charge transfer. *Appl. Phys. Lett.* **2010**, *97*, 153126.
(32) Qi, D.; Chen, W.; Gao, X.; Wang, L.; Chen, S.; Loh, K. P.; Wee, A. T. S. Surface transfer doping of diamond (100) by tetrafluorotetracyanoquinodimethane. *J. Am. Chem. Soc.* **2007**, *129*, 8084−8085.
(33) Zapata-Arteaga, O.; Perevedentsev, A.; Marina, S.; Martin, J.; Reparaz, J. S.; Campoy-Quiles, M. Reduction of the lattice thermal conductivity of polymer semiconductors by molecular doping. *ACS Energy Lett.* **2020**, *5*, 2972−2978.
(34) Liu, N.; Peters, J.; Ramu, A.; Floro, J. A.; Bowers, J. E.; Zebarjadi, M. Thermoelectric transport at F_4TCNQ-silicon interface. *APL Mater.* **2019**, *7*, No. 021104.
(35) Song, E.; Baranovskiy, A.; Xu, E.; Busani, T.; Swartzentruber, B.; Zhang, S.; Amouyal, Y.; Martinez, J. A. Manipulating thermal and electronic transports in thermoelectric Bi_2Te_3 nanowires by porphyrin adsorption. *AIP Adv.* **2018**, *8*, 105010.
(36) Zhang, Y.; Day, T.; Snedaker, M. L.; Wang, H.; Krämer, S.; Birkel, C. S.; Ji, X.; Liu, D.; Snyder, G. J.; Stucky, G. D. A mesoporous anisotropic n-type Bi_2Te_3 monolith with low thermal conductivity as an efficient thermoelectric material. *Adv. Mater.* **2012**, *24*, 5065−5070.
(37) Gordillo, J. M. S.; Morata, A.; Sierra, C. D.; Salleras, M.; Fonseca, L.; Tarancón, A. Recent advances in silicon-based nanostructures for thermoelectric applications. *APL Mater.* **2023**, *11*, No. 040702.
(38) Watts, K. E.; Clary, K. E.; Lichtenberger, D. L.; Pemberton, J. E. FTIR Spectroelectrochemistry of F4TCNQ Reduction Products and Their Protonated Forms. *Anal. Chem.* **2020**, *92*, 7154−7161.
(39) Hernández, J. A.; Ruiz, A.; Fonseca, L. F.; Pettes, M. T.; Jose-Yacamán, M.; Benitez, A. Thermoelectric properties of SnSe nanowires with different diameters. *Sci. Rep.* **2018**, *8*, 11966.
(40) Hernandez, J. A.; Fonseca, L. F.; Pettes, M. T.; Jose-Yacaman, M. Thermoelectric properties of antimony selenide hexagonal nanotubes. *Nanotechnology* **2021**, *32*, No. 095705.
(41) Pan, Z.; Lee, S. H.; Wang, K.; Mao, Z.; Li, D. Elastic stiffening induces one-dimensional phonons in thin Ta_2Se_3 nanowires. *Appl. Phys. Lett.* **2022**, *120*, No. 062201.

https://doi.org/10.1021/acs.nanolett.3c02000
Nano Lett. 2023, 23, 11395−11401